Paper 38.4

INSTANTANEOUS WHOLE FIELD MEASUREMENT OF VELOCITY AND SIZE OF AIR MICROBUBBLES IN TWO-PHASE FLOWS USING DDPIV

F. Pereira, M. Gharib, D. Dabiri , D. Modarress
California Institute of Technology
Center for Quantitative Visualization
Pasadena, California 91125

ABSTRACT

Defocusing digital particle image velocimetry (DDPIV) is the natural extension of digital particle image velocimetry (DPIV), planar or quasi three-dimensional, to a true and unique three-dimensional PIV technique. This work presents the defocusing optical concept by which the depth information can be retrieved, thus overriding the limitation to in-plane measurements of actual PIV techniques, either standard or stereo-based. The concept is implemented into a three-dimensional imaging system specifically designed for the purpose of mapping two-phase bubbly flows. Digital images of the bubble field are recorded and analysed to provide information both on the physical location of every single particle/bubble and on its respective size, which is estimated from the scattered light intensity. The calculation of the true three-component velocity field is done by local spatial cross-correlation between two consecutive sets of particle/bubble locations. The spatial resolution and uncertainty limits are established based on a simplified model of the defocusing optical system. Accuracy measurements show that the average error on the displacements is about 0.02 pixels. The methodology used to measure the size is laid out by application of the Mie scattering theory. A DDPIV prototype instrument was fabricated on specific requirements. The instrument records high resolution images of the bubble field and is capable of providing bubble size and bubble location within a cubic foot volume. The technique is applied to the study of the dynamics of sub-millimeter air bubbles in a three-dimensional vortical flow generated by a propeller. Velocity, bubble size distribution and void fraction for these flows are discussed.

1. INTRODUCTION

Air bubbles are created in large quantities in the wake of ocean vessels by propeller cavitation, by surface entrainment through free surface wave breakage by the ship's bow and stern, or by air entrainment in the turbulent boundary layer near the hull. Because of their large acoustical cross sections, they are responsible for the acoustical signature of the wake, which is known to persist for long periods of time. Larger bubbles will rise to the surface within a very short period of time, resulting in a surface slick detectable by radar or by altitude imaging devices (Griffin et al, 1992). There has been considerable interest in determining the air bubble population, thus resulting in much progress, specially in the area of bubble acoustics (Trevorrow et al, 1994) and cavitation inception (Billet, 1985). Nevertheless, the coupling between bubbles and turbulent flows is far from understood. The experimental approaches in free surface water tunnels and tow tanks can provide an insight into the field of bubbly flow dynamics. However, the turbulent, multi-phase and three-dimensional nature of the flow demands experimental capabilities beyond standard single point measurement techniques (Naqwi et al, 1991) or planar imaging systems (Prasad and Adrian, 1993; Grant et al, 1995). A non-intrusive diagnostic instrument is needed, capable of mapping the surrounding flow field and tracking the spatial and temporal history of bubbles, with sufficient sensitivity to accurately estimate the void fraction, in three dimensions and within a reasonably large volume. Existing three-dimensional techniques such as holography (Barnhart et al, 1994), neutron radiography (Mishima and Hibiki, 1998), Doppler tomographic imaging (Chen et al, 1997), particle tracking (Maas et al, 1993), multilayer particle imaging (Abe et al, 1998) or scanning particle imaging (Brucker, 1997) suffer from extreme complexity, unsufficient spatial or temporal resolution, and/or lack of capability to measure both size and velocity data. In this paper, we present an intrinsically three-dimensional imaging system based on the defocusing concept introduced by Willert and Gharib (1992). This system is capable of real-time imaging of bubbly flows, providing both bubble size and velocity information in three dimensions. In a first part, we describe the defocusing concept. In the second part, we present the accuracy measurements performed to determine the instrument performance, followed by a specific study for the size measurement. Finally, we apply the technique to map a vortical flow generated by a propeller and seeded with sub-millimeter air bubbles.

2. DEFOCUSING CONCEPT

The foundations of the defocusing concept have been established in an early paper by Willert and Gharib (1992). We report here the most important aspects in a revised form. For clarity, we will use the term *particle* when referring both to a solid particle and to a bubble.

2.1 Principle

A typical 2-D imaging system, consisting of a converging lens and of an aperture, is represented in figure 1 to help describe the Defocusing Digital Particle Image Velocimetry (DDPIV) technique. Figure 1a exhibits a point A, located on the object plane (or reference plane), and a point B placed in between this plane and the lens system. Point A appears focused in A', on the image plane (or sensor plane), while B is projected as a blurred image B'. The DDPIV technique uses a mask with two or more apertures shifted away from the optical axis to obtain multiple images from each scattering source, as shown in figure 1b. The image shift b on the image plane, caused by these off-axis apertures, is related to the depth location of the source points, whereas the scattered light intensity combined with the blurredness is used to recover the size information.

2.2 Geometric Analysis

A simplified geometric model of a two-aperture defocusing optical arrangement is represented in figure 2. The interrogation domain is defined as a cube of side a, thus a square in the plane. The back face of this cube is on the reference plane which is placed at a distance L from the lens plane. Let d be the distance between apertures, f the focal length of the converging lens and l the distance from the lens to the image plane. The image plane is materialized by a photosensor (e.g. CCD) of height h. The physical space is attached to a coordinate system originating in the lens plane, with the Z-axis on the optical axis of the system. Coordinates in the physical space are designated (X,Y,Z). The image coordinate system is simply the Z-translation of the physical system onto the sensor plane, i.e. at $Z = -l$. The coordinates of a pixel on the imaging sensor are given by the pair (x,y). Point $P(X,Y,Z)$ represents a light scattering source such as particle, bubble, point-like dot, etc. For $Z \neq L$, P is projected onto points $P'(x',y')$ and $P''(x'',y'')$, separated by the distance b.

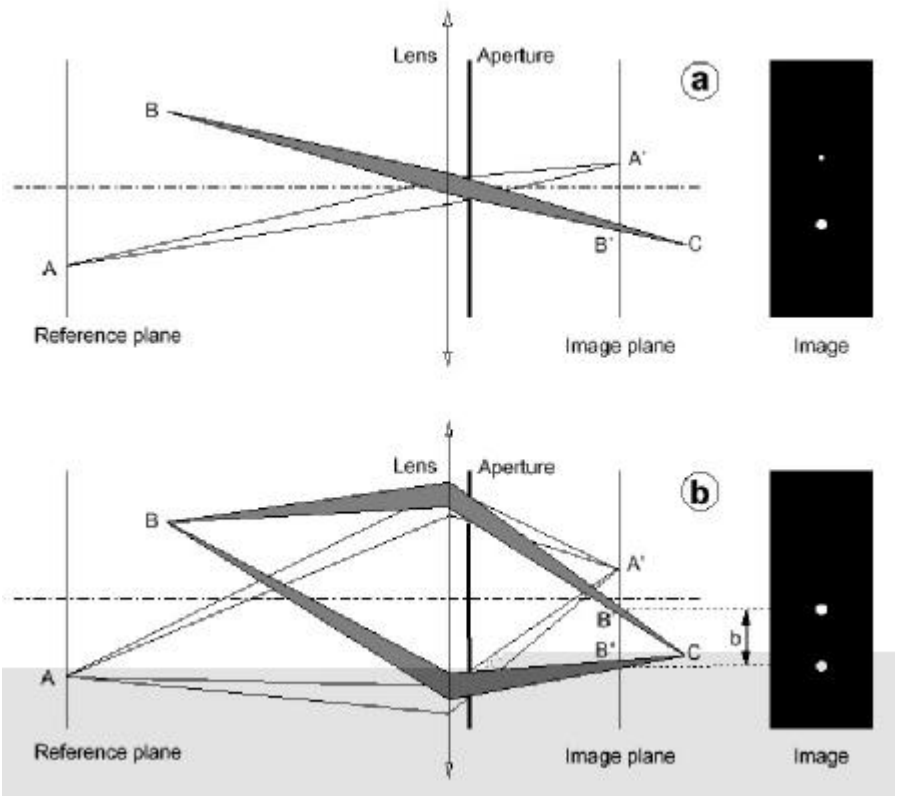

Fig 1. The defocusing principle: a) standard imaging system, b) defocusing arrangement

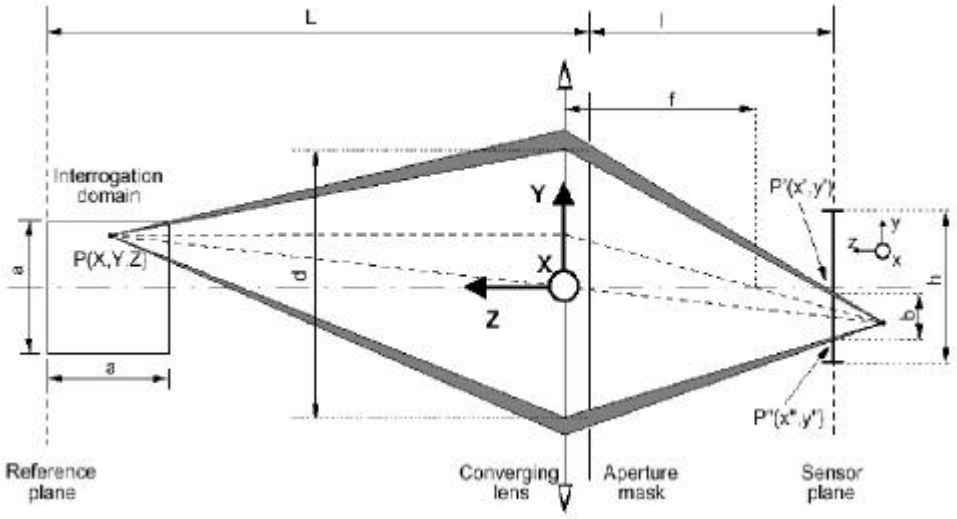

Fig 2. Simplified defocusing optical model

Image coordinates

The coordinates *(x',y')* and *(x'',y'')* of the images *P'* and *P''* of *P(X,Y,Z)* in the image plane are given by the following relations:

$$\begin{cases} x' = x'' = -ML\dfrac{X}{Z} \\ y' = \dfrac{M}{2Z}\left[d(L-Z) - 2LY\right] \\ y'' = \dfrac{M}{2Z}\left[-d(L-Z) - 2LY\right] \end{cases} \quad (1)$$

where *M* is the optical magnification provided by the lens equation.

Image separation

The image separation vector **b** represents the distance between the images *P'* and *P''*. The norm is therefore given by

$$b = \frac{Md}{Z}(L - Z) = \frac{1}{K}\left(\frac{1}{Z} - \frac{1}{L}\right) \quad with \quad K = \frac{1}{MdL} \tag{2}$$

The value *b* is reported in figure 3, nondimensionalized by the height *h* of the imaging sensor, as a function of the ration *Z/L*. Three values of *d* are considered for the aperture separation. The interrogation domain size *a* is set to *100 mm* and the focal plane is such that *L=1000 mm*. The height of the sensor is *h=10 mm* (typical for sensors of *1kx1k* pixels, for instance). The observed domain is defined by a cube whose back face is on the reference plane, but the observable and measurable domain is a volume that extends from the reference plane to a minimum *Z* position. This volume encompasses the interrogation domain defined by *a*, extending from the focal plane to a point of coordinates $(0,0,Z_{min})$ on the optical axis where *b/h* equals unity, as reported in figure 3.

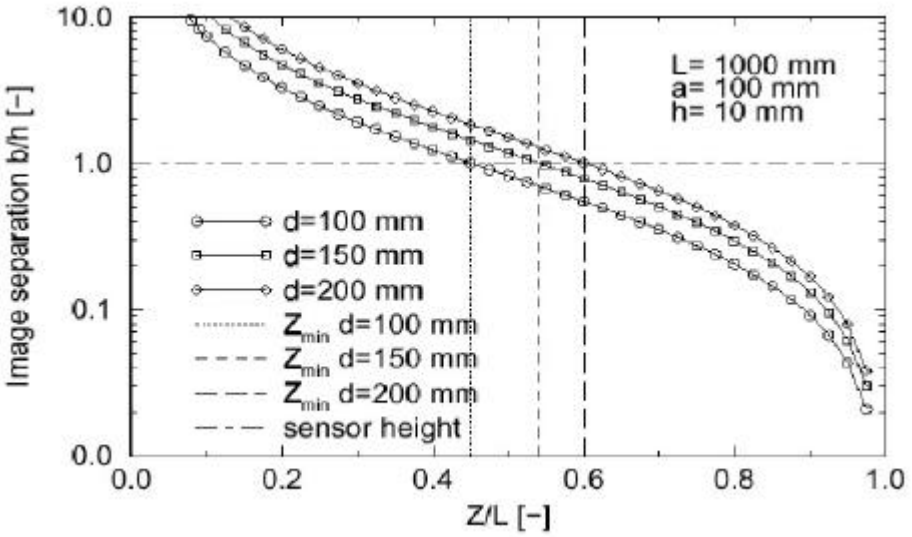

Fig 3. Image separation *b*

Equation 2 demonstrates the extreme simplicity of the defocusing concept, which of course is greatly valuable in terms of computational implementation and processing speed. In purely geometric terms, the image separation *b* is independent of the in-plane coordinates *X* and *Y*. Likewise, the pinhole diameter has no bearing on *b* and is only responsible for the amount of blurredness of any given particle image. It is important to note that these observations are only valid if the system is free of optical aberrations. These aberrations are divided into two classes: focusing aberrations (spherical aberration, astigmatism and coma), which induce magnification errors; image distortion, which creates a nonlinear relationship between the actual location of the particle and its location on the image (i.e. the magnification varies as a function of the position in the field of the image). In particular, increased aberrations are likely to occur with increased separation *b*.

From equation 2, *b* is negative for *Z>L* and reverts sign for *Z£L*. In other terms, the image pattern defined by the image pair *P'* and *P''* flips orientation when the object point *P* crosses the reference plane. For a two-aperture design as depicted in figure 2, this result leads to a non-uniqueness problem because *b* is a monotonically decreasing function with increasing *Z*: the sign of *b* cannot be determined unequivocably from the image information. To overcome this ambiguity, one can either use distinct shapes for the apertures or use multiple apertures. For our prototype instrument, we use three pinholes, arranged into a triangular pattern. This configuration, shown in figure 4, exhibits a flipping triangle when *P* moves across the reference plane and requires straightforward and fast image processing routines.

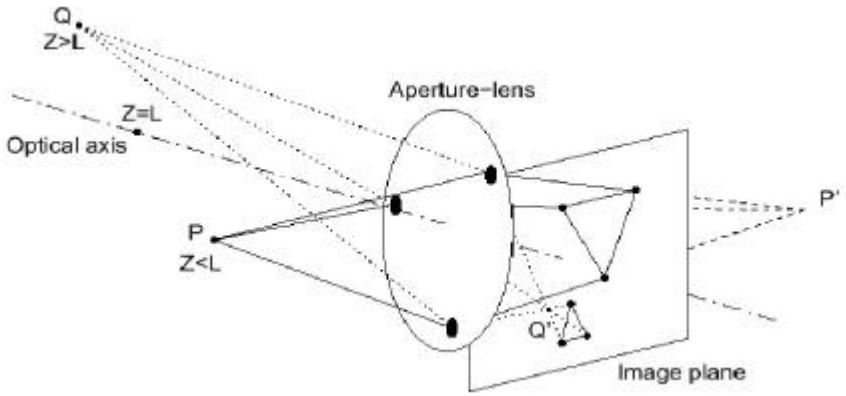

Fig 4. Three-aperture arrangement

The sensitivity of the system, i.e. its ability to detect small changes of the particle location, can be evaluated through the separation gradient

$$\frac{\partial b}{\partial Z} = -\frac{1}{KZ^2} \tag{3}$$

This gradient is reported in figure 5 versus *Z/L*, for the same values of *L*, *a* and *h* as above, and for different distances *d* between apertures. Because of the nature of *b*, ¶*b*/¶*Z* increases monotonically with *Z* and is independent of the in-plane components, with an asymptotic behavior when approaching the reference plane. The distance *d* between the apertures is a critical parameter. Increased *d* induces an increased sensitivity of *b* on Z variations, but this has a negative counterpart on the limits of the working domain, which is delimited on one end by the reference plane and on the other end by Z_{min}. This value is also reported on the plot for the three values of *d* and is seen to approach *L* with increasing *d*, thus confining the interrogation area to lower sensitivity conditions. However, the separation between apertures should be kept as large as possible for optimum performance.

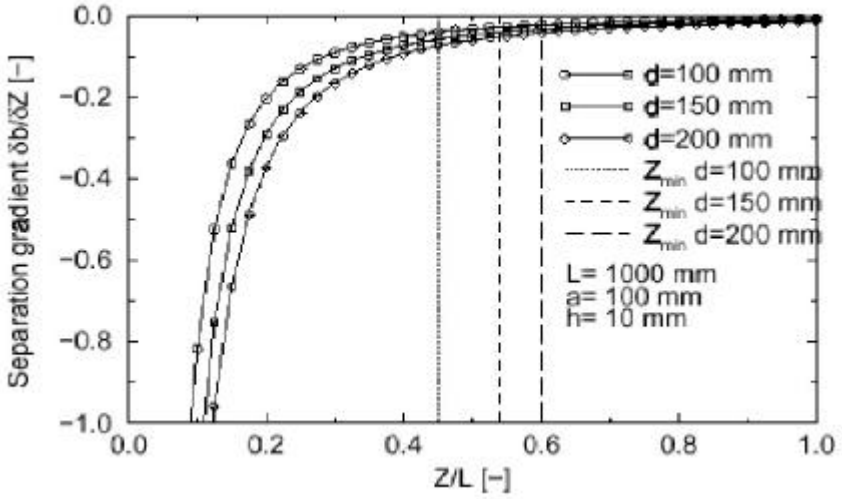

Fig 5. Image separation gradient

Space coordinates

The coordinates of *P* in the world coordinate system are derived from the image coordinates of the projections *P′* and *P″*, see equations 1:

$$\begin{cases} X = -\dfrac{x_0 Z}{ML} & with \quad x_0 = \dfrac{x' + x''}{2} \\ Y = -\dfrac{y_0 Z}{ML} & with \quad y_0 = \dfrac{y' + y''}{2} \\ Z = \dfrac{1}{\dfrac{1}{L} + Kb} \end{cases} \tag{4}$$

Assuming that the apertures are equidistant from the origin of the coordinate system, the image point defined by (x_0,y_0) is the image of the particle if there were a single aperture at the origin.

2.3 Uncertainty Analysis

A measure of the overall performance of the system can be defined by considering the ratios between the individual error components, thus giving dimensionless terms that can be used as a comparison criterion between different systems or as a guide criterion in the design stage as to meet the resolution requirements. In PIV techniques the depth component is derived from in-plane information (i.e. the image). For this reason, the ratio between the out-of-plane and the in-plane error components is a first choice (see e.g. Prasad and Adrian, 1993). For the defocusing DPIV technique, we show using standard errors procedures, that the spatial uncertainties in the object space can be written as

$$\begin{aligned} \frac{\delta(dZ)}{\delta(dX)} &= \frac{\dfrac{Z}{d}}{\sqrt{\dfrac{1}{2} + \left(\dfrac{X}{d}\right)^2}} \\ \frac{\delta(dZ)}{\delta(dY)} &= \frac{\dfrac{Z}{d}}{\sqrt{\dfrac{1}{4} + \left(\dfrac{Y}{d}\right)^2}} \end{aligned} \tag{5}$$

where d is the uncertainty on a given variable.

Let e_r be the ratio $d(dZ)/d(dY)$ defined above. Interestingly, equations 5 show that e_r depends exclusively on one and only one geometric parameter: the distance d between apertures. e_r is reported in figure 6 as a function of the off-axis position Y/d and for different distances Z/d. e_r is symmetric about the centerline $(Y/d=0)$, where it reaches a maximum value. e_r falls away from the centre of the field of view.

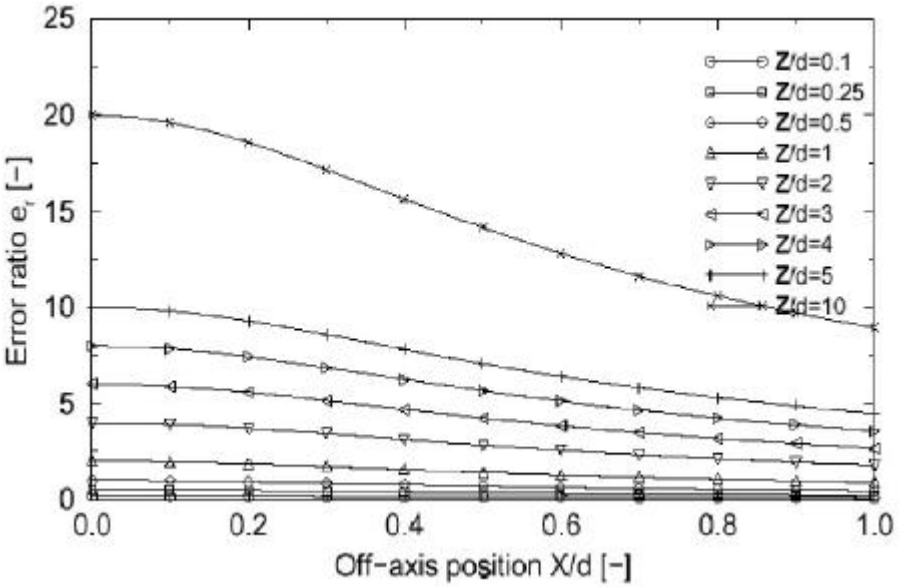

Fig 6. Error ratio e_r versus off-axis position Y/d for different distances to camera Z/d

The influence of the parameter d on e_r is clearly stated in figure 7, where e_r is plotted against the ratio d/Z for $Y/d=0$ (centerline). For a given location Z, the best performance is obtained for larger d.

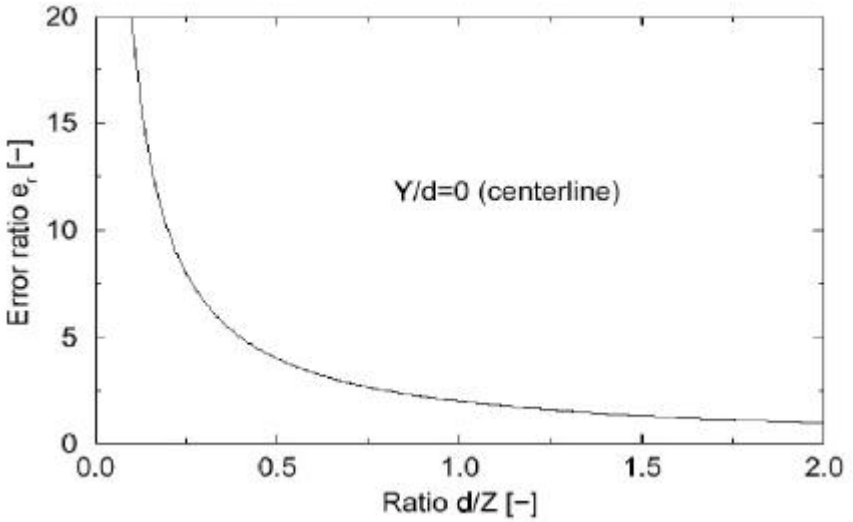

Fig 7. Error ratio e_r versus ratio *d/Z, Y/d=0* (centerline)

3. ACCURACY ASSESSMENT

A camera system has been designed and fabricated based upon the above analysis. The specific characteristics of this instrument can be found in the paper by Pereira et al (1999). The DDPIV spatial accuracy and velocity accuracy are addressed hereafter.

3.1 Spatial location

A 12"x12" glass plate with a grid pattern of dots is used and moved along the *Z*-axis by increments of *10 mm* by means of a motorized translation stage. Figure 8 represents, at each station along the *Z*-axis, the in-plane and out-of-plane mean error and standard deviation, respectively. The average errors on the *X-Y* plane and on the *Z* direction are found to be *42 mm* and *658 mm*, respectively. With the magnification *M*, the in-plane error corresponds in the image plane to 0.08 pixel, whereas the out-of-plane error represents about 1.3 pixels.

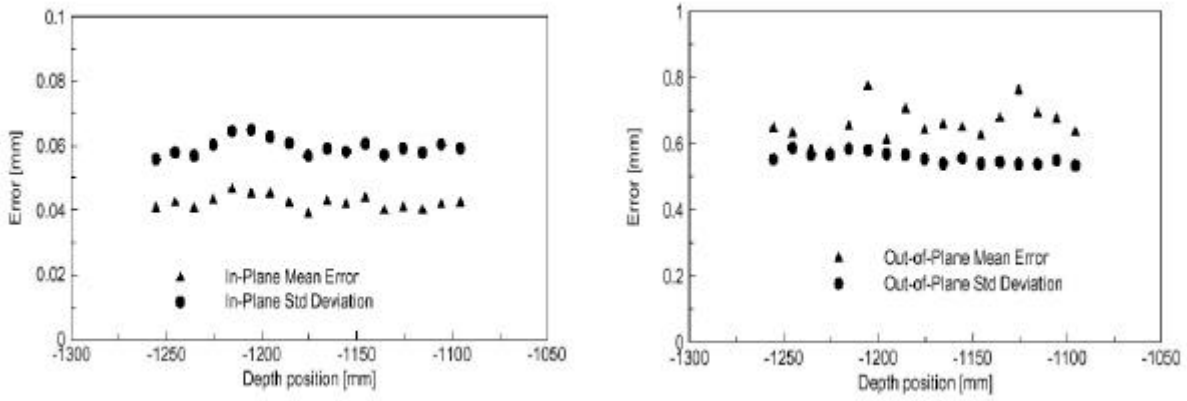

Fig 8. Left: in-plane errors; right: out-of-plane errors

3.2 Velocity

The velocity vector field is obtained by local spatial cross-correlation between small volume elements (*voxels*) containing particles observed at two time steps, as described by Pereira et al (1999). The velocity accuracy is established using a flat and rigid disk of *300 mm* in diameter and put into rotation. The disk is tilted in space to cover the full interrogation domain. The tangential velocity is set to *1 m.s*$^{-1}$ at the outer radius. Figure 9 shows the absolute mean error and the root mean square error on the displacement corresponding to the measured velocity, plotted against the actual displacement. Both are expressed in terms of pixel displacements. The mean error on the displacement is below 0.05 pixel. The *rms* error is found to increase almost linearly with the reference displacement. Indeed, the cross-correlation procedure provides the most probable displacement in any given voxel. Moreover, the computed velocity vector is positioned at the center of the corresponding voxel. For these reasons and because the measurements are performed using a purely rotating flow, the *rms* error increases with the observed displacement.

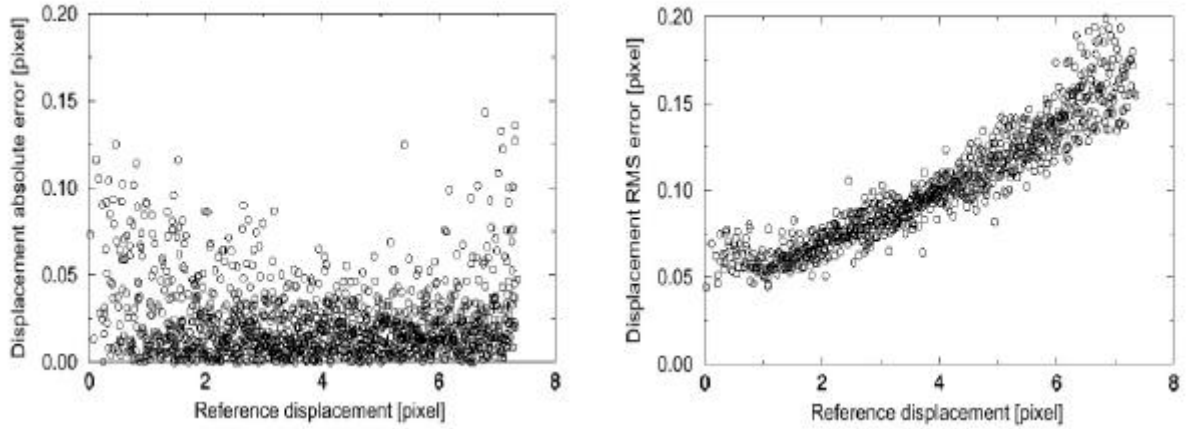

Fig 9. Left: displacement absolute error; right: displacement rms error

4. SIZE MEASUREMENT

The Lorenz-Mie theory provides the exact solution to the problem of scattering of light by a single, homogeneous sphere of arbitrary size (Van De Hulst, 1957). This theory relates the particle/bubble scattering intensity to the sphere size. Although the Mie solution is difficult to apply, it can be approached by geometrical optics

In this study, the size measurement procedure consists of measuring the intensity of the light scattered by calibrated glass microspheres. Seven diameters are considered: *99.6, 200, 278, 400, 480, 756* and *1008 mm.* A matrix of these microspheres is immersed into a water tank and moved along the camera Z-axis. Let I_0 be a reference intensity value. Figure 10 displays the normalized intensity I/I_0 averaged over all *Z* positions versus the sphere radius *a*. The log-log representation exhibits a power law relationship. The power of the fitting curve *(»1.92)* is found to correspond to the theoretical value of *2* derived from the Mie scattering theory and found experimentally by other researchers (Landa and Tebay, 1970). This result suggests that one could use such a relation to make effective and accurate size measurements based on the particle/bubble intensity, provided a reference intensity is available at every location in the interrogation volume. An in-depth procedure, similar to that used by (Hofeldt and Hanson, 1991), should be performed to complete these preliminary results. Finally, as one would expect from the spatial accuracy measurements presented earlier, the spatial resolution of the current DDPIV system is here clearly bounded to radii no larger than *100 mm.* One can overcome this limit by using higher resolution and higher sensitivity image sensors.

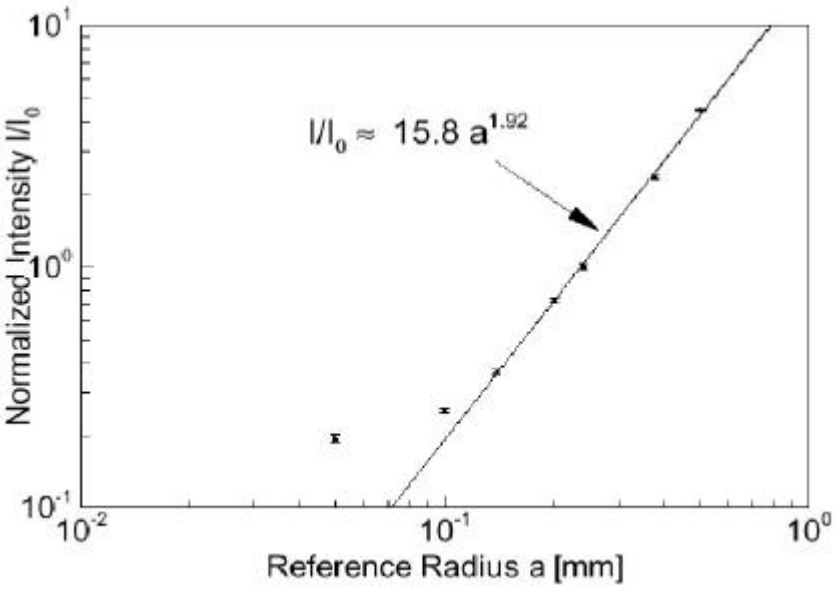

Fig 10. Normalized scattered intensity versus reference radius a and power fit

5. APPLICATIONS

5.1 Case 1

A two-blade model boat is immersed into water tank. The rotation speed is *12 rps,* corresponding to a tangential velocity of *2.52* $m.s^{-1}$ at the tip of the blades. A bubble generator below the propeller, producing a dense stream of rising sub-millimeter air bubbles. The velocity field is obtained through phase averaging.

A 3-D velocity field is obtained after averaging and outlier correction. Massless particles are then artificially injected into the mean velocity data set, in a radial arrangement and one diameter upstream the propeller. Paths of bubbles are determined, providing an unique insight into this complex flow as shown in figure 11. Color/gray level relates to the local measured velocity amplitude. Velocity reaches a maximum of *2.49 m.s*$^{-1}$ in the outer region of the propeller, matching closely the blade tip tangential velocity.

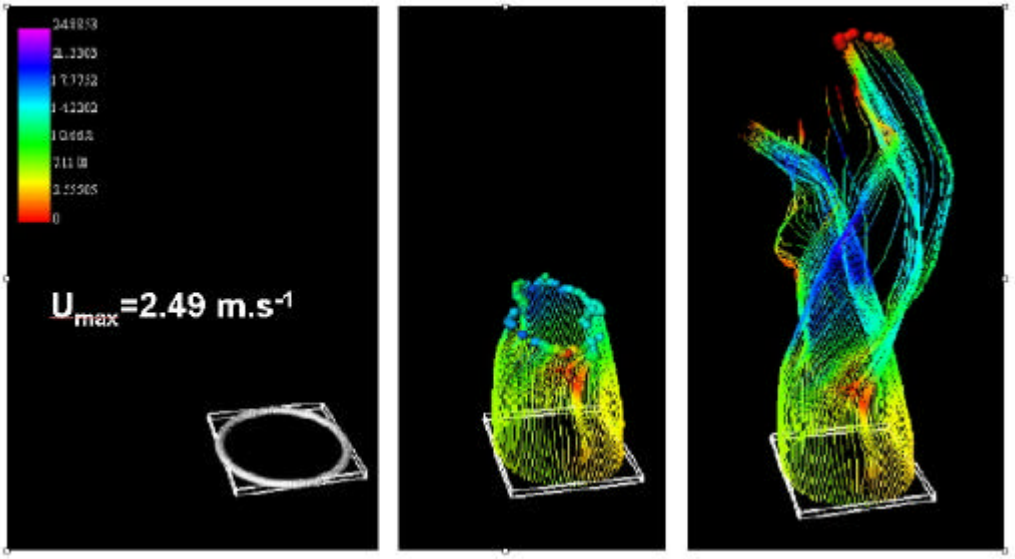

Fig 11. Pathlines of bubbles around the propeller

The bubble mean radius along the *Y* vertical axis of the flow (rotation axis of the propeller) is reported in figure 12. The mean radius increases almost linearly to almost *325 mm* at *Y»30 mm*, where the propeller is located. After the bubbles pass the immediate vicinity of the propeller, the radius is found to follow the opposite trend, decreasing to about *200 mm*. The growth of bubbles is partly due, but to a very small extent, to the decrease of the static pressure with increasing *Y*. In fact, bubbles experience first the low pressure in the suction side of the propeller before getting into the high pressure region where they collapse.

In the same figure, we report the histograms calculated taking the same bubble population below and above *Y=30 mm*. The histogram peak follows the trend outlined before due to the pressure variations. The ratio of the upstream to the downstream populations is *65%*. However, the ratio of the respective void fractions is close to *100%*. These observations indicate that coalescence of bubbles is the main mechanism acting here, although breakup may occur in the propeller region.

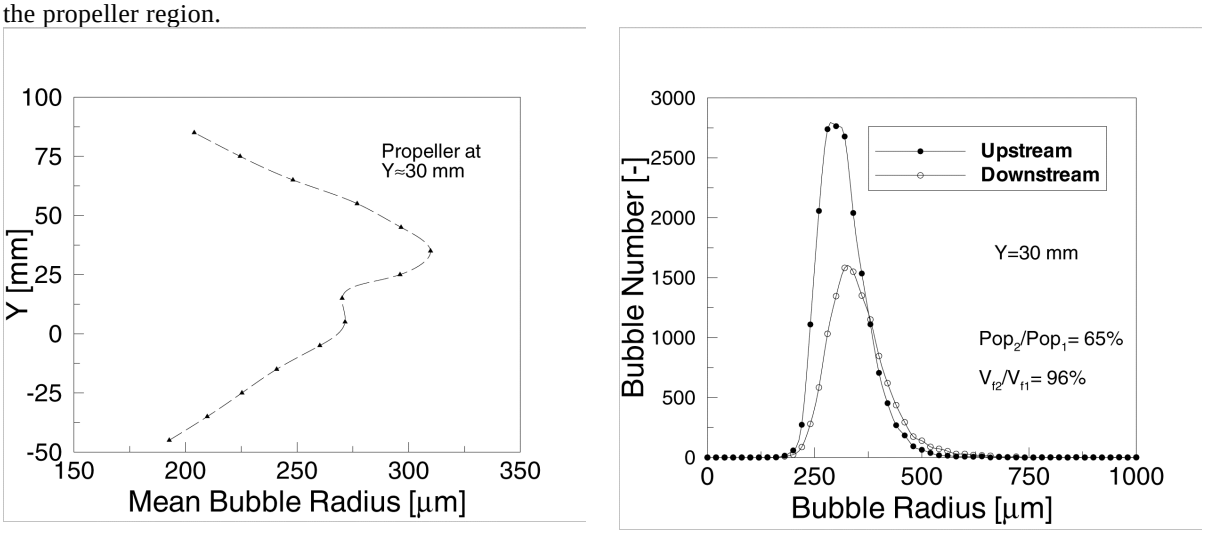

Fig 12. Left: bubble mean radius versus *Y*; right: size distribution upstream and downstream section *Y=30 mm*

5.2 Case 2

A similar configuration is used here. A three-blade model boat propeller is rotated at *12 Hz*. The velocity field represented in figure 13 is obtained by phase-averaging a sequence of 50 instantaneous velocity fields. Spurious vectors can be seen on borders of the interrogation domain. A slice in the velocity field, as shown in figure 14, clearly displays the high speed jet core along the downstream section of the propeller axis. However, the isovelocity contours displayed on the same figure show a viscous wake that appears as a velocity defect due to the merging of the two boundary layers from the blades. A slight contraction of the slipstream could also be detected. The wake is found to rapidly fade into the

bulk flow. Presently, work is being performed on every aspect of this flow that should carry out new results, along with interesting comparisons with works from other researchers (e.g., Hyun and Patel, 1991; Stella et al, 2000).

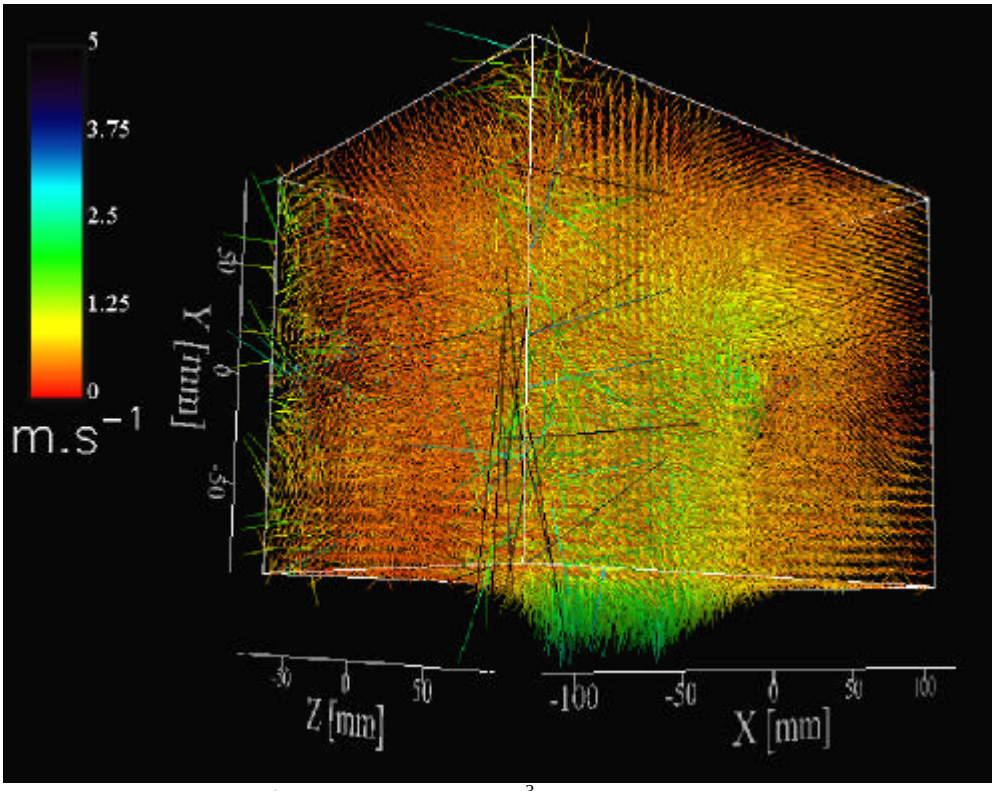

Fig 13. Velocity field: 200x200x400 mm^3, 72963 vectors (33*33*67 voxels)

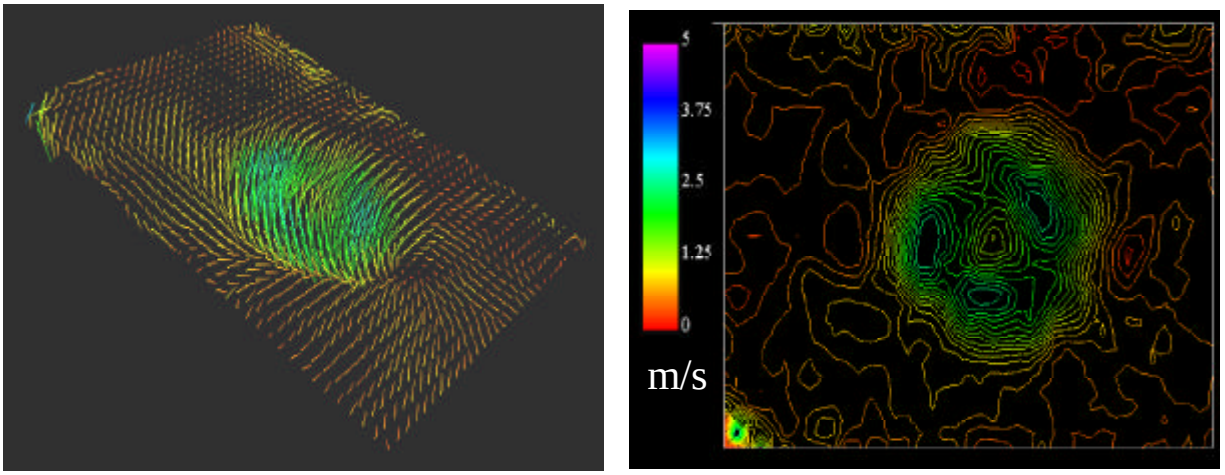

Fig 14. Left: velocity cross-section (downstream region, 0.5 diameter); right: corresponding isovelocity contours

6. CONCLUSION AND PERSPECTIVES

The defocusing concept has been analysed, from the geometric point of view and a detailed error analysis has been performed. The prototype instrument designed upon this analysis has an in-plane location error of 0.08 pixels and an out-of-plane location error of 1.3 pixels. In terms of velocity calculation, we found a mean absolute error of less that 0.05 pixels on the displacement evaluation through the three-dimensional spatial cross-correlation. procedure. Very encouraging results also show that particle/bubble size can be accurately determined using the scattered light intensity of particles. Good agreement was found with the Mie Scattering theory and work is being performed to extend the range of size measurement. Application to a bubbly flow around a propeller provided a remarkable insight into this complex flow. The variations of the mean bubble size were detected as the bubbles were entrained through the propeller. The analysis of the bubble size histograms and of the void fractions upstream and downstream the propeller clearly pointed out that coalescence was the major bubble collective interaction mechanism in this flow. Contraction of the slipstream and velocity defect due to the viscous wake could also be observed.

ACKNOWLEDGMENTS

The visit of Dr. F. Pereira to the C.Q.V. was made possible by a fellowship of *the Fundação para a Ciência e a Tecnologia*, Portugal. The research was supported by the Office of Naval Research (contract N00014-97-1-0303), under the direction of Dr. Edwin P. Rood and Dr. Mark Hyman. The Defocusing Digital Particle Image Velocimetry (DDPIV) technology is protected under a U.S. pending patent filed by California Institute of Technology.

REFERENCES

Abe M; Yoshida N; Hishida K; Maeda M (1998) Multilayer PIV Technique with High Power Pulse Laser Diodes. In proc. 9th Int. Symp. Appl. Laser Tech. Fluid Mech., Lisbon, Portugal

Barnhart DH; Adrian RJ; Papen GC (1994) Phase-Conjugate Holographic System for High-Resolution Particle Image Velocimetry. Applied Optics 33(30):7159-7170

Billet ML (1985) Cavitation Nuclei Measurements – A Review. In Proc. Cavitation and Multiphase Flow Forum, pp. 31-38, Albuquerque, NM

Brücker C (1997) 3D Scanning PIV Applied to an Air Flow in a Motored Engine Using Digital High Speed Video. Meas Sci Technol 8: 1480-1492

Chen Z; Milner TE; Dave D;Nelson JS (1997) Optical Doppler Tomographic Imaging of Fluid Flow Velocity in Highly Scattering Media. Opt lett 22: 64-66

Grant I; Fu S; Pan X; Wang X (1995) The Application of an In-line, Stereoscopic, PIV System to 3-Component Velocity Measurements. Exp. Fluids 19:214-221

Griffin OM; Peltzer RD, Reed AM; Beck RF (1995) Remote Sensing of Surface Ship Wakes. Naval Engineers Journal pp.245-258

Hofeldt DL; Hanson RK (1991) Instantaneous Imaging of Particle Size and Spatial Distribution in Two-Phase Flows. Applied Optics 30(33):4936-4948

Hyun BS; Patel VC (1991) Measurements in the Flow Around a Marine Propeller at the Stern of an Axisymmetric Body. Exp Fluids 11: 33-44

Landa I; Tebay ES (1970) The Measurement and Instantaneous Display of Bubble Size Distribution, Using Scattered Light. In Proc. 5th Cavitation Forum, Detroit, MI

Maas HG; Gruen A; Papantoniou D (1993) Particle Tracking Velocimetry in Three-Dimensional Flows. Exp Fluids 15: 133-146

Mishima K; Hibiki T (1998) Development of High-Frame-rate Neutron Radiography and Quantitative Measurement Method for Multiphase Flow Research. Nuclear Eng Design 184: 183-201

Naqwi A; Durst F; Kraft G (1991) Sizing of Submicrometer Particles Using a Phase-Doppler System. Applied Optics 30(33): 4903-4913

Pereira F; Gharib M; Dabiri D; Modarress D (1999) Defocusing DPIV: A 3-Component 3-D DPIV Measurement Technique. Application to Bubbly Flows. Submitted to Exp Fluids

Prasad AK; Adrian RJ (1993) Stereoscopic Particle Image Velocimetry Applied to Liquid Flows. Exp. Fluids 15:49-60

Stella A; Guj G; Di Felice F (2000) Propeller Wake Flowfield Analysis by Means of LDV Phase Sampling Techniques. Exp Fluids 28: 1-10

Trevorrow MV; Vagle S; Farmer DM (1994) Acoustical Measurements of Microbubbles Within Ship Wakes. J Acoust Soc Am 95(4): 1922-1930

Van de Hulst HC (1957) Light Scattering by Small Particles. Wiley, New York